J|A|C|S
ARTICLES
Published on Web 11/04/2006

# (*n*,*m*) Abundance Evaluation of Single-Walled Carbon Nanotubes by Fluorescence and Absorption Spectroscopy

Zhengtang Luo,[†] Lisa D. Pfefferle,[§] Gary L. Haller,[§] and Fotios Papadimitrakopoulos*,[†]

*Contribution from the Nanomaterials Optoelectronics Laboratory, Department of Chemistry, Polymer Program, Institute of Materials Science, University of Connecticut, Storrs, Connecticut 06269, and Department of Chemical Engineering, Yale University, New Haven, Connecticut 06520*

Received August 7, 2006; E-mail: papadim@mail.ims.uconn.edu

***Abstract:*** A methodology that takes into account the (*n*,*m*) structure of single-walled carbon nanotubes (SWNTs), through an exciton−exciton resonance model and an electron−phonon interaction model, was employed in order to evaluate the semiconducting (*n*,*m*) abundance of two SWNT samples (i.e., Co−MCM-41 and HiPco). This was based on photoluminescence and near-infrared absorption data obtained on aqueous suspensions of individually dispersed SWNTs. In the absence of known (*n*,*m*) abundance SWNT samples, we resorted to determining the diameter distribution curves for both samples, which were found to obey an unsymmetrical log-normal distribution, typical for vapor-phase particle growth. Using this log-normal function, we reconstructed the near-infrared $E^{S}_{11}$ absorption spectrum of the narrow diameter distribution Co−MCM-41 SWNT sample, which in turn enabled us to assess the predictions of these two theoretical models. High spectral reconstruction accuracy was obtained from the electron−phonon interaction model when considering (11,0) and (10,0) zigzag nanotubes, along with (*n*,*m*) line widths inversely proportional to their extinction coefficients.

## Introduction

Single-walled carbon nanotubes (SWNTs), identified by their chiral indices (*n*,*m*) or equivalently their diameter ($d_t$) and chiral angle ($\theta$), are widely recognized as potential building blocks for future nanoscale electronics.[1] At present, the ability to characterize (*n*,*m*) SWNT abundance in a given sample is hindered due to the unavailability of some of the "basic" properties of these materials, such as extinction coefficients and quantum yields for each (*n*,*m*) SWNT. Recent studies indicate that these parameters are strongly dependent on not only nanotube diameter and chirality but also modality (i.e., mod-($n-m$,3)).[2,3] While photoluminescence (PL)[4,5] and tunable-laser excitation resonance Raman spectroscopy (RRS) on debundled and individually isolated SWNTs have enabled the combined assignment of the majority of (*n*,*m*) SWNTs,[6−9] precise determination of their relative abundance remains elusive. Such debundling and individual solubilization of SWNTs was realized using a variety of surfactants, such as sodium dodecyl sulfate (SDS),[4] sodium dodecylbenzene sulfonate (SDBS),[10] and DNA.[11] No profound diameter or chiral angle selectivity was reported for surfactants SDBS and DNA, while enhanced sample stability and higher SWNT concentrations can be obtained with the latter surfactant.[12]

Among these two characterization techniques, PL spectroscopy provides a quick and easy identification for the majority of semiconducting (*sem*-) (*n*,*m*) SWNTs.[5,13−15] Corresponding measurements on similar samples using the more laborious tunable-laser RRS technique indicated that, along with the different metallic (*met*-) (*n*,*m*) SWNTs, a number of additional semiconducting SWNTs were present, mostly low-chiral-angle zigzag (*n*,0) nanotubes.[6,8,16] Recent theoretical studies indicate

[†] University of Connecticut.
[§] Yale University.

(1) Dresselhaus, M. S., Dresselhaus, G., Avouris, P., Eds. *Carbon Nanotubes: Synthesis, Structure, Properties, and Applications*; Topics in Applied Physics 80; Springer: Berlin, 2001; p 447.
(2) Reich, S.; Thomsen, C.; Robertson, J. *Phys. Rev. Lett.* **2005**, *95*, 077402/1−077402/4.
(3) Oyama, Y.; Saito, R.; Sato, K.; Jiang, J.; Samsonidze, G. G.; Grueneis, A.; Miyauchi, Y.; Maruyama, S.; Jorio, A.; Dresselhaus, G.; Dresselhaus, M. S. *Carbon* **2006**, *44*, 873−879.
(4) O'Connell, M. J.; Bachilo, S. M.; Huffman, C. B.; Moore, V. C.; Strano, M. S.; Haroz, E. H.; Rialon, K. L.; Boul, P. J.; Noon, W. H.; Kittrell, C.; Ma, J.; Hauge, R. H.; Weisman, R. B.; Smalley, R. E. *Science* **2002**, *297*, 593−596.
(5) Bachilo, S. M.; Strano, M. S.; Kittrell, C.; Hauge, R. H.; Smalley, R. E.; Weisman, R. B. *Science* **2002**, *298*, 2361−2366.
(6) Fantini, C.; Jorio, A.; Souza, M.; Strano, M. S.; Dresselhaus, M. S.; Pimenta, M. A. *Phys. Rev. Lett.* **2004**, *93*, 147406/1−147406/4.
(7) O'Connell, M. J.; Sivaram, S.; Doorn, S. K. *Phys. Rev. B: Condens. Matter Mater. Phys.* **2004**, *69*, 235415/1−235415/15.
(8) Telg, H.; Maultzsch, J.; Reich, S.; Hennrich, F.; Thomsen, C. *Phys. Rev. Lett.* **2004**, *93*, 177401/1−177401/4.
(9) Luo, Z.; Doorn, S. K.; Papadimitrakopoulos, F. *Appl. Phys. Lett.* **2006**, *88*, 073110.
(10) Moore, V. C.; Strano, M. S.; Haroz, E. H.; Hauge, R. H.; Smalley, R. E.; Schmidt, J.; Talmon, Y. *Nano Lett.* **2003**, *3*, 1379−1382.
(11) Zheng, M.; Jagota, A.; Semke, E. D.; Diner, B. A.; McLean, R. S.; Lustig, S. R.; Richardson, R. E.; Tassi, N. G. *Nat. Mater.* **2003**, *2*, 338−342.
(12) Zheng, M.; Jagota, A.; Strano, M. S.; Santos, A. P.; Barone, P.; Chou, S. G.; Diner, B. A.; Dresselhaus, M. S.; McLean, R. S.; Onoa, G. B.; Samsonidze, G. G.; Semke, E. D.; Usrey, M.; Walls, D. J. *Science* **2003**, *302*, 1545−1548.
(13) Lefebvre, J.; Homma, Y.; Finnie, P. *Phys. Rev. Lett.* **2003**, *90*, 217401/1−217401/4.
(14) Lebedkin, S.; Hennrich, F.; Skipa, T.; Kappes, M. M. *J. Phys. Chem. B* **2003**, *107*, 1949−1956.
(15) Miyauchi, Y.; Chiashi, S.; Murakami, Y.; Hayashida, Y.; Maruyama, S. *Chem. Phys. Lett.* **2004**, *387*, 198.

that nanotubes with smaller $\theta$ possess weaker PL intensities than do nanotubes with higher $\theta$, among other differences according to modality, family (i.e., $2n+m$ = const), and diameter that further complicate ($n,m$) abundance evaluation.[2,3] At present, there is a considerable controversy over whether the extremely weak PL intensities of zigzag nanotubes originate from their lower quantum yield or low abundance values due to their unstable cap structures (especially for small $d_t$ nanotubes), both of which adversely affect their growth.[3]

Most recently, two theoretical models (based on exciton−exciton resonance model[2] and single-particle tight-binding (TB) theory,[3] hereafter referred to as the "electron−phonon interaction model") have surfaced that provide analytical predictions about the relative PL quantum efficiency and absorption extinction coefficients of various ($n,m$) SWNTs. Similarly, the electron−phonon interaction model has been utilized to develop a correlation between resonance Raman radial breathing mode (RBM) cross sections and $E^S_{22}$ PL excitation intensities, toward abundance evaluation for given ($n,m$) SWNTs.[17,18] In addition, transmission electron microscopy (TEM) has been utilized to correlate nanotube diameter distribution with PL intensities.[19] The lack, however, of well-defined samples containing known amounts of given ($n,m$) SWNTs hinders our ability to verify the validity of these and future models and furthermore utilize them in evaluating ($n,m$) abundances of unknown samples.

In this work, we employ PL spectroscopy to investigate two chemical vapor deposition (CVD) samples synthesized using carbon monoxide disproportionation. The first sample is the widely used HiPco nanotubes with broad diameter ($d_t$) distribution that displays 36 different *sem*-($n,m$) SWNTs in its PL spectra. The second sample was synthesized from cobalt-infiltrated MCM-41 mesoporous catalyst (Co−MCM-41) SWNT and displays a narrow diameter distribution with 13 *sem*-($n,m$) SWNTs in its PL spectra. Using the aforementioned two theoretical models along with the experimentally obtained relative PL intensities, an "apparent" ($n,m$) abundance was extracted for the two samples that enabled us to determine that their diameter distributions obey a log-normal function. Using such a log-normal distribution function, we then reconstructed the $E^S_{11}$ absorption manifold of the narrowly $d_t$-distributed Co−MCM-41 SWNT sample and compared the predictions of these two models against the highly resolved, experimentally obtained near-infrared absorption spectrum. This enables us to (1) spectroscopically pinpoint the presence of zigzag nanotubes that are not observed in PL measurements and (2) develop a rational methodology to assist the convergence of both theoretical models and experimental sample preparation toward the accurate determination of semiconducting ($n,m$) SWNT abundance.

## Experimental Section

**Chemicals.** Single-stranded DNA (GT)20, purified by standard desalting, was purchased from Alpha DNA Inc. Deuterium oxide ($D_2O$, 99.9 atom % D) was purchased from Acros Organics. Sodium dodecylbenzene sulfonate (SDBS, purity >99.0%) was purchased from Aldrich Chemical Co. All chemicals were used as received, unless otherwise stated.

**Preparation of SWNT Samples.** Co−MCM-41 SWNTs were synthesized from cobalt-incorporated MCM-41 catalyst templated with C12 alkyl chains as published elsewhere.[20] After their synthesis, the Co−MCM-41 SWNT sample was purified in NaOH, followed by HCl, and then followed by filtration and washing with deionized water. High-pressure monoxide (HiPco) SWNTs were grown and purified using an established method.[21]

**Preparation of Aqueous, Individually Isolated SWNT Suspensions.** Suspensions of individually isolated SWNTs were prepared using single-stranded DNA $(GT)_{20}$ for Co−MCM-41, while HiPco SWNTs were suspended using SDBS in $D_2O$, according to Zheng et al.[12] and O'Connell et al.,[4] respectively. The $D_2O$/surfactant/SWNT mixture was then sonicated using a cup-horn ultrasonicator (Cole-Palmer) for 10 min. After ultrasonication, the suspension was centrifuged for 2−4 h at ca. 80000*g* to remove the catalyst particles and big bundles.

**Characterization Methods.** Fluorescence spectroscopy measurements were conducted on a Jobin-Yvon Spex Fluorolog 3-211 spectrofluorometer equipped with a PMT near-infrared (NIR) detector. The intensities were corrected for instrumental variations in excitation intensity and detection sensitivity. The room-temperature UV−vis−NIR absorption spectra were obtained on a Perkin-Elmer Lambda-900 UV−NIR spectrometer.

## Result and Disscussion

Figure 1a illustrates a two-dimensional PL excitation map for the aqueous dispersion of Co−MCM-41 SWNT/DNA with excitation scanned from 300 to 930 nm and emission collected from 800 to 1550 nm. The excitation photons create excitons in the appropriate $E^S_{ii}$ (index $i$ refers to $i$th sub-band and "S" denotes semiconducting SWNTs), which then relax to the lowest sub-band ($E^S_{11}$) to recombine and emit light.[5] The resonance behavior of both excitation and emission events results in the spikes in Figure 1a, which correspond to the transition pair from individual ($n,m$) SWNTs.[5] The spectral peak positions from Figure 1a are plotted in Figure 1b, where the size of dots is proportional to their PL intensities. The unassigned dots above those assigned to (7,5) and (6,5) in Figure 1b are the sidebands of exciton−phonon bound states,[22] respectively, which will be studied in more detail in future publications. The region between 1.65 and 2.48 eV (or 750 and 500 nm) excitation energies corresponds to the pair of $E^S_{22}$ absorption and $E^S_{11}$ emission. This absorption/emission pair is flanked by two dashed-line rectangles containing, at the top, the $E^S_{33}/E^S_{11}$and $E^S_{44}/E^S_{11}$ pairs and, at the bottom, the $E^S_{11}/E^S_{11}$ pair.[5] The ($n,m$) assignment of each peak was obtained following the methodology of Bachilo et al.[5] The geometrical patterns for the ($2n+m$) = constant families of 17, 19, 20, 22, and 23 are clearly shown with the numbers in squares. These families are clustered into groups of different modality (i.e., mod($n-m$,3) = 1 for the ($2n+m$) families of 17, 20, and 23, while the 19 and 22 families belong to mod($n-m$,3) = 2) that are placed to the left and right of the blue dashed line, respectively. ($n,m$) SWNTs that have pair transitions to the left of the blue dashed line (mod1) exhibit $E^S_{22}/E^S_{11}$ ratios larger than the slope of the line (ca. 1.73), while those to the right (mod2) have a ratio smaller than 1.73. In the

(16) Doorn, S. K.; Heller, D. A.; Barone, P. W.; Usrey, M. L.; Strano, M. S. *Appl. Phys. A: Mater. Sci. Process.* **2004**, *A78*, 1147−1155.
(17) Jorio, A.; Fantini, C.; Pimenta, M. A.; Heller, D. A.; Strano, M. S.; Dresselhaus, M. S.; Oyama, Y.; Jiang, J.; Saito, R. *Appl. Phys. Lett.* **2006**, *88*, 023109/1−023109/3.
(18) Jorio, A.; Fantini, C.; Pimenta, M. A.; Capaz, R. B.; Samsonidze, G. G.; Dresselhaus, G.; Dresselhaus, M. S.; Jiang, J.; Kobayashi, N.; Gruneis, A.; Saito, R. *Phys. Rev. B: Condens. Matter Mater. Phys.* **2005**, *71*, 075401/1−075401/11.
(19) Okazaki, T.; Saito, T.; Matsuura, K.; Ohshima, S.; Yumura, M.; Oyama, Y.; Saito, R.; Iijima, S. *Chem. Phys. Lett.* **2006**, *420*, 286−290.
(20) Chen, Y.; Ciuparu, D.; Lim, S.; Yang, Y.; Haller, G. L.; Pfefferle, L. *J. Catal.* **2004**, *225*, 453−465.
(21) Nikolaev, P.; Bronikowski, M. J.; Bradley, R. K.; Rohmund, F.; Colbert, D. T.; Smith, K. A.; Smalley, R. E. *Chem. Phys. Lett.* **1999**, *313*, 91−97.
(22) Plentz, F.; Ribeiro, H. B.; Jorio, A.; Strano, M. S.; Pimenta, M. A. *Phys. Rev. Lett.* **2005**, *95*, 247401/1−247401/4.

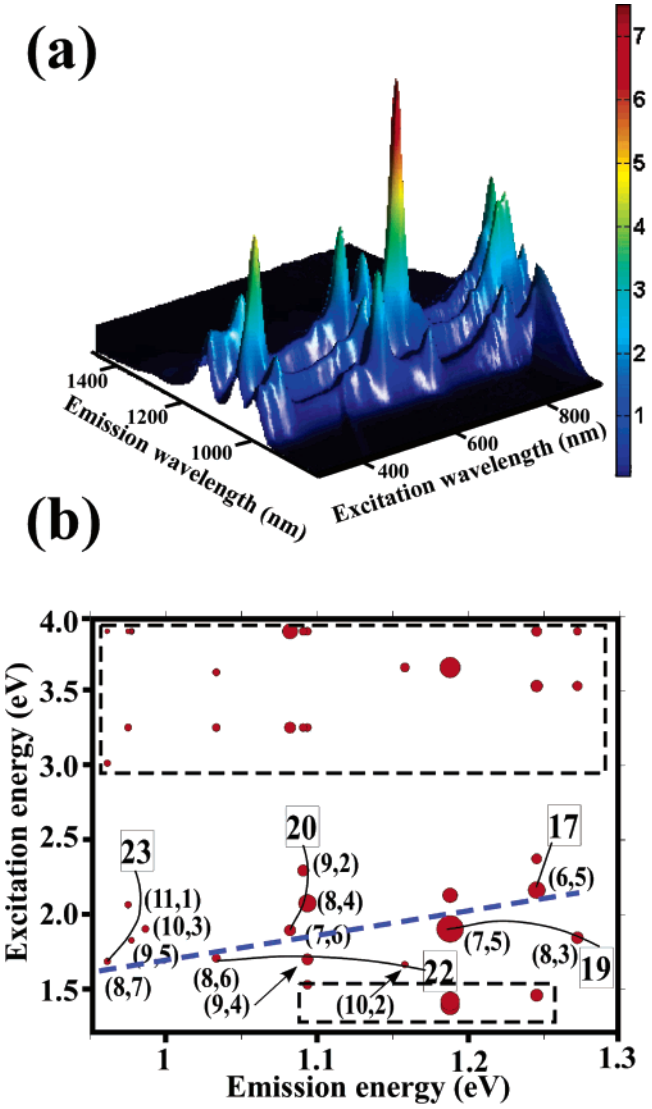


***Figure 1.*** (a) Photoluminescence excitation (PLE) intensity map as a function of excitation and emission wavelength for DNA-micellarized Co−MCM-41 SWNT sample in $D_2O$. Data are interpolated using MATLAB. (b) $(n,m)$ and $(2n+m)$ family (dashed box) assignment of the PLE spectra shown in panel a. Dot size is proportional to intensity. Dashed-line rectangles at the top and bottom enclose partial ($E_{33}$ and $E_{44}$) and $E_{11}$ transitions, respectively. The straight dashed blue line (slope = 1.73) indicates the near-armchair direction, with nanotubes above and below corresponding to mod1 and mod2 species, respectively.

case of the Co−MCM-41 SWNTs of Figure 1, the (7,5) SWNT, which is a mod2 nanotube, shows the highest PL intensity. For the HiPco SWNT samples (Table S1, Supporting Information), the dominant PL peaks appear to originate from the (7,5), (7,6), (8,3), (8,4) (8,6), (8,7), and (10,3) SWNTs.

Figure 2 illustrates the chirality map for both SWNT samples, along with their respective diameters ($d_t = (a/\pi)(n^2 + m^2 + nm)^{1/2}$) in nanometers. The Co−MCM-41 sample contains 13 different semiconducting $(n,m)$ SWNT species, shown with green hexagons. The HiPco sample contains 36 semiconducting SWNTs, enclosed by a solid red line. This map indicates that the Co−MCM-41 SWNTs possess a quite sharp $(n,m)$ distribution. This control is attributed to size stabilization of the Co catalyst within the MCM-41 framework, leading to a narrow diameter distribution of the resulting SWNTs.[20]

A tempting assumption would be to linearly correlate the $E^{S}_{22}$ excitation intensity with the concentration of $(n,m)$ SWNTs. In the following discussion, correcting the experimentally observed PL intensities will be demonstrated using both the aforementioned exciton−exciton resonance model[2] and the electron−phonon interaction model.[3] Figure S1 and S2, as well as Table S2, in the Supporting Information present the calculated values for both PL ($I^{PL}_{cal}(n,m)$) and absorption ($I^{abs}_{cal}(n,m)$) intensities as a function of diameter, modality, and $(2n+m)$ family pattern.[2,3] While both models predict that the PL intensities (and corresponding absorbencies) are strongly dependent on their $(2n+m)$ families and modalities, considerable deviations in the calculated results are observed. This signifies the importance of correlating the experimentally observed PL intensities ($I^{PL}_{exp}(n,m)$) with those derived theoretically ($I^{PL}_{cal}(n,m)$) in order to accurately determine the $(n,m)$ abundance in a given nanotube sample. With this in mind, it is imperative to recognize the differences between these two models, which could ultimately enable us to pinpoint both strengths and weaknesses. In particular, significant intensity variations in these two models are observed with (a) chirality, (b) modality for low-chiral-angle nanotubes, and (c) overall intensity decrease from small to large diameters, as shown in Figure S1 in the Supporting Information.

The abundance, $A(n,m)$, of a particular $(n,m)$ SWNT can then be calculated from the following equation,

$$A(n,m) = C\frac{I^{PL}_{exp}(n,m)}{I^{PL}_{cal}(n,m)} \quad (1)$$

where $C$ is a normalization factor and $I^{PL}_{exp}(n,m)$ and $I^{PL}_{cal}(n,m)$are the experimentally obtained and calculated PL intensities of the corresponding $(n,m)$ SWNTs, respectively, when in resonance (i.e., when the energy of the excitation light matches the $E^{S}_{22}$).

Figure 3 illustrates the histograms of diameter distribution of Co−MCM-41 and HiPco SWNTs that were calculated using eq 1 and $I^{PL}_{cal}(n,m)$ data sets from the exciton−exciton resonance model[2] and the electron−phonon interaction model.[3] Interestingly, the diameter distributions of both samples and, in particular, the narrow-distribution samples (i.e., Co−MCM-41 SWNTs), regardless of the PL model employed, show a skewed shape with a step rise at smaller sizes of the distribution and a long tail at larger sizes of the distribution. This is consistent with the distribution obtained by TEM[19,21] and $E^{S}_{22}$ RRS RBM analysis,[18] which is contrary to the widely assumed symmetric Gaussian distributions, although small deviations in the resulting $(n,m)$ abundance might originate from varying CVD growth conditions. This line shape closely matches the characteristics of single-mode log-normal distribution, which has the following form,

$$A(d_t) = \frac{1}{d_t\sqrt{2\pi}\ln\sigma}\exp\left[-\frac{1}{2(\ln\sigma)^2}[\ln(d_t) - \ln(\mu)]^2\right] \quad (2)$$

where $A(d_t)$ is the abundance at diameter $d_t$, $\mu$ is the geometric mean diameter, and $\sigma$ is the dimensionless geometric standard deviation, which determines the shape of the distribution. CVD-grown particles are often found to exhibit log-normal size distribution.[23] The unsymmetrical log-normal characteristic of

(23) Soderlund, J.; Kiss, L. B.; Niklasson, G. A.; Granqvist, C. G. *Phys. Rev. Lett.* **1998**, *80*, 2386−2388.

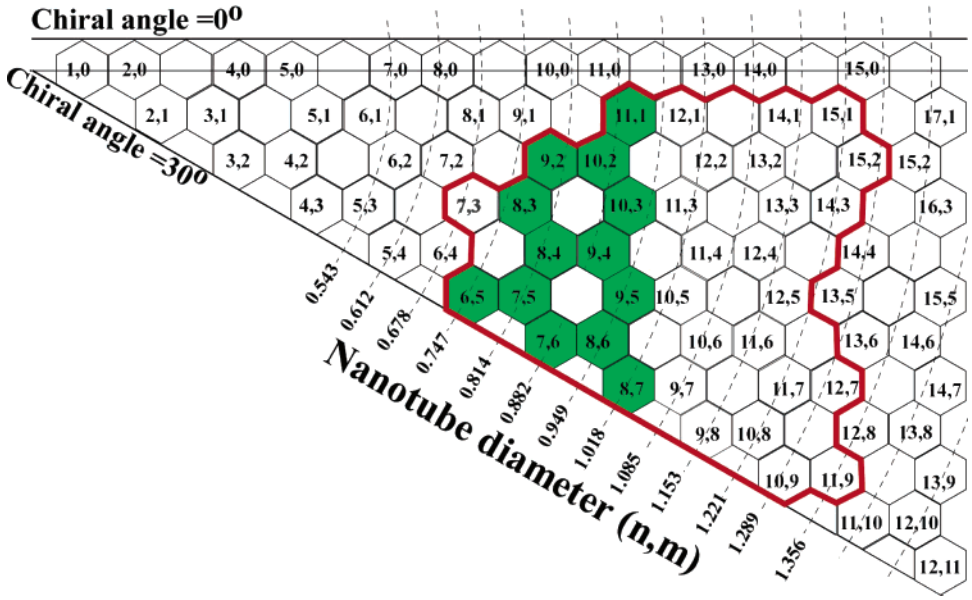


***Figure 2.*** Chirality maps of aqueous suspensions of Co−MCM-41 (green hexagons) and HiPco SWNTs (enclosed by solid red line).

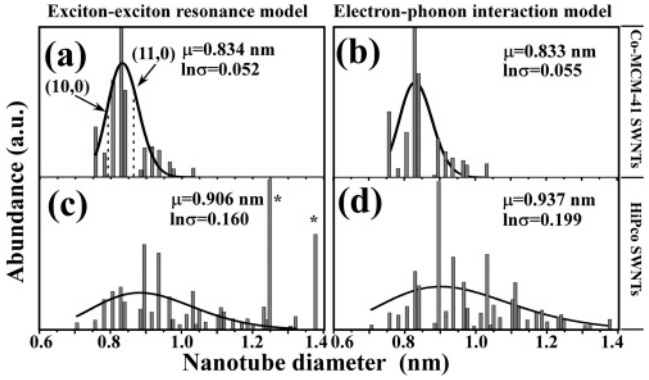


***Figure 3.*** Calculated diameter distribution histograms (bars) and their log-normal fits arranged horizontally for two samples and vertically for the two models of calculated PL intensity values. Asterisks indicate an inaccuracy of the exciton−exciton resonance model to correctly predict the abundance for large-diameter SWNTs. These nanotubes were not included in the curve fitting. Dashed lines in panel a indicate the positions of the (10,0) and (11,0) zigzag SWNTs.

diameter distribution for both nanotube samples, apart from the employed PL model, indicates that the catalyst nanoparticles might obey the log-normal distribution of classically CVD-grown inorganic nanoparticles. However, we must point out that another scenario might be at play, where the $I^{PL}_{cal}(n,m)$ values for small-diameter nanotubes are underestimated in both models, as a result of excitonic enhancement in tighter confinement.[17]

Significant differences in the abundance profiles as a function of diameter can be observed from Figure 3, and these differences are accentuated for the samples with wider diameter distribution. For example, the geometric mean diameters ($\mu$) for HiPco SWNTs were predicted to be 0.906 and 0.937 nm according to the exciton−exciton resonance model and the electron−phonon interaction model, respectively, where the latter is closer to the reported 0.93 nm value.[5] This discrepancy originates from the aforementioned variation in the overall decrease of the relative PL intensities from small- to large-diameter nanotubes predicted by the two models. For example, the PL intensities for 1.2−1.3 nm $d_t$ nanotubes are between 30−10% and 20−10% for the exciton−exciton resonance model and the electron−phonon interaction model, respectively, as shown in Figure S1 and Table S2 in the Supporting Information. This undervalues the abundance of large-$d_t$ nanotubes for the exciton−exciton resonance model and places the exciton−exciton resonance model at a disadvantage with respect to the electron−phonon interaction model. Moreover, as can be seen in Figure 3c, the nanotube abundances for (14,3) and (11,9) (marked with asterisks), belonging to $(2n+m) = 31$ and mod2 species, are predicted to be oddly higher under the exciton−exciton resonance model. This provides an additional indication that the exciton−exciton resonance model leads to certain inaccuracies in predicting of PL intensities for larger diameter nanotubes.

To further investigate the abundance-prediction strengths of these two theoretical models, spectral reconstruction of the $E^S_{11}$ NIR absorption spectrum of the narrowly $d_t$-distributed Co−MCM-41 SWNTs was performed to interrogate the strengths and weaknesses of these two models. These models provide us with a comprehensive set of $E^S_{22}$ absorption extinction coefficients for all the ($n$,$m$) SWNTs, including the zigzag ($n$,0) nanotubes, which are not observed in PL. Unlike $E^S_{22}$, however, the reconstruction of the $E^S_{11}$ spectrum manifold is significantly more straightforward, as the various ($n$,$m$) transitions are spread out over a wider range, and additionally as the $E^S_{11}$ absorptions are situated at the end of the plasmonic and scattering tail, thereby making background subtraction easier. For this, we assumed that the $E^S_{11}$ absorption extinction coefficients are proportional to the $E^S_{22}$ values provided by the two theoretical models, based on the results calculated by Popov et al., who observed similar absorption matrix element patterns for the $E^S_{11}$ and $E^S_{22}$ transitions.[24] Mie theory suggests that the scattering and absorption cross section of particles is a power series of the size parameter $\beta$, related to absorption wavelength ($\lambda$) and particle dimension ($R_s$) ($\beta = 2\pi R_s/\lambda$).[25] In the wavelength region far from the plasmonic resonance maximum (ca. 270 nm), the scattering efficiency depends more on $\beta$ than on $R_s$.[25] For this we can simply scale the plasmonic tail in the NIR absorption

(24) Popov, V. N.; Henrard, L.; Lambin, P. *Phys. Rev. B* **2005**, *72*, 035436.
(25) Hiemenz, P. C.; Rajagopalan, R. *Principles of Colloid and Surface Chemistry*, 3rd ed.; Marcel Dekker: New York, 1997; pp 232−235.

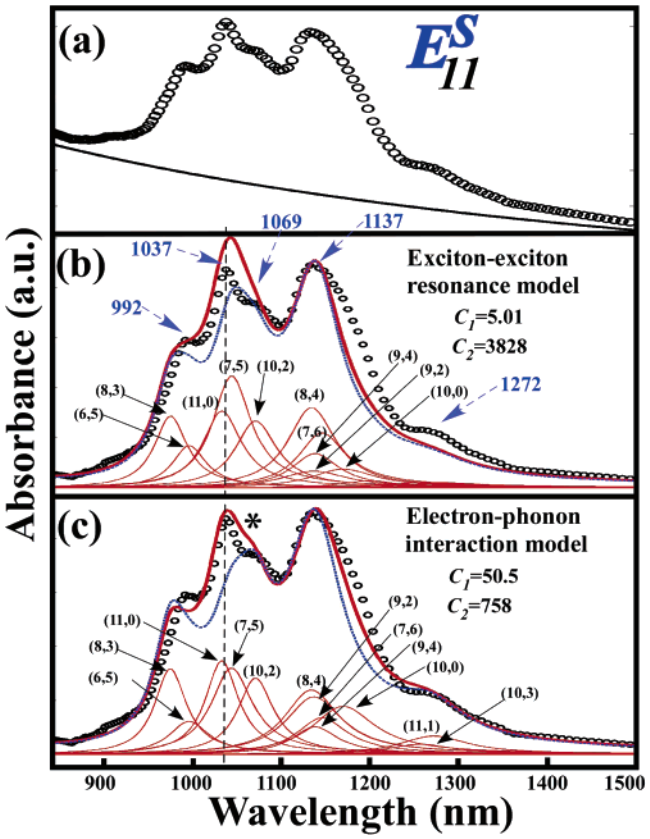


***Figure 4.*** (a) Experimental $E^S_{11}$ optical absorption spectrum (circles) and power-law-fitted background curve (solid line) of aqueous DNA-dispersed Co−MCM-41 SWNT suspensions. The spectra indicated with circles in panels b and c were obtained by subtracting the two curves in panel a. (b,c) Spectral reconstruction by the summation of the thin Lorentzian peak contribution from each (*n*,*m*) SWNT, calculated using the exciton−exciton resonance model and the electron−phonon interaction model, respectively. The thick dashed line and solid line depict the sum of all Lorentzian lines with and without the (10,0) and (11,0) zigzag nanotubes, respectively. Dashed arrows refer to features of interest in the experimental spectrum. The asterisk in panel c indicates the 1069 nm shoulder that was reproduced in the reconstructed spectrum.

of Figure 4a by a power law (i.e., $\sim A\lambda^{-b}$), where the *b* value was obtained from the optimum fit of the background signal and found to be 0.7609. The circles and solid line in Figure 4a illustrate the NIR $E^S_{11}$ absorption spectra of a DNA-wrapped, individually isolated Co−MCM-41 SWNT sample in $D_2O$ suspension and the power law fit described above.

Although the Voigt profile (a combination of Gaussian and Lorentzian functions) for each (*n*,*m*) SWNT species is widely used in fitting of the fluorescence and absorption spectra and a better fitting can be obtained, we choose to use the Lorentzian profile for the spectral reconstruction to reduce the number of adjustable parameters. The overall contribution to the expected optical density (OD) of all (*n*,*m*) SWNTs at a specific optical energy *E* can be calculated by using the following equation,

$$\mathrm{OD}(E) = C\sum_{n,m} A(\mathrm{d}_t) I^{\mathrm{abs}}_{\mathrm{cal}}(n,m) \frac{\gamma_e}{4(E - E_{11}(n,m))^2 + \gamma_e^2} \quad (3)$$

where *C* is the normalization factor introduced to account for sampling conditions and the collection geometries. $I^{\mathrm{abs}}_{\mathrm{cal}}(n,m)$ values for $E^S_{11}$ transitions are taken from the calculated $E^S_{22}$ extinction coefficients (as described above) for either the exciton−exciton resonance model or the electron−phonon interaction model (see Table S2 and Figure S2 in the Supporting Information). $E_{11}(n,m)$ values were obtained from the PLE measurements of Figure 1 (with no Stokes's shift applied), and $\gamma_e$ is the width of the optical transitions, which is related to the lifetime of the excited state. The $E_{11}(n,m)$ values for the zigzag nanotubes (i.e., (10,0) and (11,0)) were obtained from ref 2. Here, the log-normal diameter distribution function, $A(d_t)$, for the Co−MCM-41 SWNT sample, obtained in Figure 3a,b, was used, such that the relative abundance of weak-fluorescence nanotubes, in particular the zigzag (11,0) and (10,0) SWNT with $d_t$ of 0.862 and 0.783 nm, can also be introduced. This presents one extreme case, where *no* diameter-induced chirality is imparted by the catalyst. The other extreme case corresponds to the complete absence of (10,0) and (11,0) zigzag nanotubes, with the actual Co−MCM-41 SWNT sample more likely to fall between these two extremes.

At the beginning, spectral reconstruction was performed by optimizing a single parameter ($\gamma_e$), which was kept the same for all (*n*,*m*) SWNTs. Figure S3 in the Supporting Information illustrates the spectral reconstruction of the $E^S_{11}$ absorption for the exciton−exciton resonance model and the electron−phonon interaction model in the presence and in the absence of the two zigzag nanotubes. The surprisingly good fit obtained with such a single adjustable parameter ($\gamma_e = 65$ meV) is a testament to the viability of this approach. As will be described below, the inclusion of the two zigzag nanotubes is important for reproducing the experimental $E^S_{11}$ absorption spectrum. However, upon closer inspection of the reconstruction fidelity, we realized that maintaining a single $\gamma_e$ value for all (*n*,*m*) SWNTs is insufficient to properly reproduce the 992, 1069, and 1272 nm shoulders. In particular, the 1069 nm shoulder (marked with an asterisk in Figure 4c) is virtually impossible to generate with a single $\gamma_e$ value. As predicted by the Strickler−Berg formula,[26] for a molecule with very well resolved vibronic structure, the inverse of radiative lifetime is linearly proportional to the extinction coefficient to for a homogeneously broadened system. On this basis, we can simply couple the $\gamma_e$ value of a given (*n*,*m*) nanotube with its absorption extinction coefficients. For this, we can approximate $\gamma_e = C_1 + C_2/I^{\mathrm{abs}}_{\mathrm{cal}}(n,m)$ and spectrally reconstruct the $E^S_{11}$ absorption spectrum using two (i.e., $C_1$ and $C_2$) adjustable parameters, as opposed to one ($\gamma_e$). Figure 4, panels b and c, presents the results of the reconstructed $E^S_{11}$ absorption spectrum based on the exciton−exciton resonance model and the electron−phonon interaction model, respectively. The electron−phonon interaction model (Figure 4c), which includes the (11,0) and (10,0) zigzag nanotubes, provides the best match to the experimentally obtained absorption curve. In particular, the 1069 nm absorption shoulder is accurately reproduced (underneath the asterisk in Figure 4c), along with the 992 and 1272 nm shoulders. The emergence of the 1069 nm shoulder is attributed to the high extinction coefficients of the (11,0) and (10,2) nanotubes that reduce their line widths ($\gamma_e$ inversely proportional to $I^{\mathrm{abs}}_{\mathrm{cal}}(n,m)$) and generate this feature. The re-appearance of the 1069 nm feature after coupling the lifetime variation on each (*n*,*m*) SWNT emphasizes the need to better understand line width variation with respect to the rest of the optical properties. Moreover, the closer match in the 1140−1220 nm region for the electron−phonon interaction

(26) Strickler, S. J.; Berg, R. A. *J. Chem. Phys.* **1962**, *37*, 814−822.

model, as opposed to the exciton−exciton resonance model, implies that the former theory better describes the overall absorption behavior with respect to diameter and chirality (see Figure S2 in the Supporting Information). The resulting $\gamma_e$ values range from 58 to 96 meV for the exciton−exciton resonance model, versus 45−73 meV for the electron−phonon interaction model. These are in good agreement with the ca. 60 meV value obtained from resonance Raman experiments[6,9,27] and only slightly higher than the ∼30 meV value reported by Jones et al.[28] and O'Connel et al. for SDS-encapsulated SWNTs solution.[4] This discrepancy might originate from environmental effects related to inhomogeneous DNA coverage (estimated $\gamma_e$ values ∼40 meV for DNA-dispersed SWNTs[11]), since the line widths for surfactant-free (air-suspended) nanotubes are on the order of 10−15 meV.[13]

The inclusion of the (11,0) and (10,0) zigzag nanotubes (i.e., one extreme) is particularly important to obtain an optimum reconstruction. If they are removed (the other extreme), the maximum 1037 nm absorbance shifts to the 1069 nm shoulder, which results in a poorer spectral match. Based on intensity variations between the experimental and reconstructed spectra in Figures 4 and S3, the actual sample appears to lie somewhere between these two extremes and, according to the current spectral reconstruction, closer to the first case. This might be due to the large population of (11,0) SWNTs ($d_t = 0.862$ nm), which together with the (10,0) SWNTs ($d_t = 0.783$ nm) are close to the geometric mean diameter of this sample ($\mu = 0.83$ nm) (see Figure 3a). This is further amplified by the small $d_t$ distribution of the Co−MCM-41 SWNT sample and the fact that these two zigzag nanotubes carry considerable weight for their absorption footprint to go unnoticed. This is in agreement with the resonance Raman spectroscopy studies reported by Fantini et al.[6] (where (10,0) SWNTs were observed) and Telg et al.[8] (where strong signals from (11,0), (13,0), and (15,0) were observed in HiPco SWNT samples). The apparent large concentration of (10,0) and (11,0) SWNTs might also be influenced by the initial growth of the cap within the Co−MCM-41 mesoporous catalyst as opposed to HiPco SWNT synthesis. More detailed work is currently underway to clarify this, as well as to reconstruct the NIR absorption spectrum of the HiPco SWNT sample, which involves a significantly larger set of (*n*,*m*) species.

The apparent success of such a spectral reconstruction technique is believed to originate from (i) the narrow diameter distribution of the Co−MCM-41 SWNT sample, (ii) the use of the theoretically derived $I^{abs}_{cal}(n,m)$ values (which reflect the chirality and diameter contributions to the absorbance), (iii) the incorporation of the log-normal diameter distribution, and (iv) the extinction-coefficient-dependent $\gamma_e$ values. As shown in Figure 4b,c, both reconstructed spectra shown a small Stokes's shift (<8 meV), in agreement with previous reports,[28] which is due to the rigidity of the SWNTs. To the best of our knowledge, this is the first time that such a spectral reconstruction methodology has been employed, and based on our results, it shows a strong promise for quantitative nanotube abundance characterization. Obtaining a better handle on the $\gamma_e$ variation for different (*n*,*m*) nanotubes[7] would ultimately permit a closer match to the experimental absorption spectrum. Unfortunately, the large number (36) of different *sem*-SWNTs, along with more than four zigzag *sem*-SWNTs of unknown abundance and various errors associated with background subtraction, makes such reconstruction challenging and will be studied in subsequent publications.

## Conclusion

Utilizing photoluminescence and near-infrared absorption results, a quantitative methodology was developed to provide abundance profiles for all semiconducting (*n*,*m*) SWNTs within a given sample. This was based on predictions of the exciton−exciton resonance model and the electron−phonon interaction model as applied to broad (HiPco) and narrowly (Co−MCM-41) distributed SWNT samples, respectively. Our results indicate that the diameter distributions of both of these CVD-grown nanotube samples obey a log-normal distribution that is typical for a vapor-phase particle growth process. Using such a log-normal distribution function, the NIR $E^S_{11}$ absorption spectrum was accurately reconstructed with two adjustable parameters in conjunction with the theoretically derived (*n*,*m*)-dependent extinction coefficients. These two adjustable parameters were necessary in order to account for the lifetime variation in a homogeneously broadened system, which is inversely proportional to the extinction coefficient of each (*n*,*m*) SWNT. Using this methodology on the narrowly distributed Co−MCM-41 SWNT sample, our current analysis indicates that the single-particle electron−phonon interaction model provides a better overall description of nanotube optical properties according to diameter, chirality, modality, and family patterns, as opposed to the exciton−exciton resonance model. Moreover, strong evidence is presented for the existence of zigzag nanotubes in the Co−MCM-41 SWNT sample, which are not seen in the photoluminescence measurements. This provides a rational methodology toward assessing semiconducting (*n*,*m*) SWNT abundance with high accuracy, while at the same time verifying the validity and confidence level of various theoretical models.

**Acknowledgment.** The authors acknowledge helpful discussions with Profs. R. Bruce Weisman, Daniel Resasco, and Lewis Rothberg. Data in Table S1 were kindly provided by Mr. John-David Rocha and Prof. R. Bruce Weisman. We also acknowledge financial support from AFOSR FA9550-06-1-0030 and ARO-DAAD-19-02-1-10381 for Z.L. and F.P., as well as DOE-BES grant DE-FG02-05ER15732 and DARPA Contract HR0011-06-C-0011 for L.D.P. and G.L.H.

**Supporting Information Available:** Tabulated values of the relative photoluminescence intensities for a sample of HiPco SWNT in aqueous SDBS suspension; calculated absorption and PL intensities from the exciton−exciton resonance model and the electron−phonon interaction model, as well as their tabulated values; and comparative experimental and reconstructed UV−vis−NIR spectra using the same value of $\gamma_e$ for all (*n*,*m*) nanotube species. This material is available free of charge via the Internet at http://pubs.acs.org.

JA0657096

(27) Luo, Z.; Li, R.; Kim, S. N.; Papadimitrakopoulos, F. *Phys. Rev. B: Condens. Matter Mater. Phys.* **2004**, *70*, 245429/1−245429/8.
(28) Jones, M.; Engtrakul, C.; Metzger, W. K.; Ellingson, R. J.; Nozik, A. J.; Heben, M. J.; Rumbles, G. *Phys. Rev. B: Condens. Matter Mater. Phys.* **2005**, *71*, 115426/1−115426/9.